Dimple drainage before the coalescence of a droplet deposited on a smooth substrate

Laurent Duchemin[a,1] and Christophe Josserand[b]

[a]Physique et Mécanique des Milieux Hétérogènes, CNRS, ESPCI Paris, Université PSL, Sorbonne Université, Université de Paris, F-75005 Paris, France; [b]Aix Marseille Université, CNRS, Centrale Marseille, Institut de Recherche sur les Phénomènes Hors Equilibre, 13013 Marseille, France; and [c]LadHyX, UMR 7646 CNRS and Ecole Polytechnique, Institut Polytechnique de Paris, 91128 Palaiseau, France

Thin liquid or gas films are everywhere in nature, from foams to submillimetric bubbles at a free surface, and their rupture leaves a collection of small drops and bubbles. However, the mechanisms at play responsible for the bursting of these films is still in debate. The present study thus aims at understanding the drainage dynamics of the thin air film squeezed by gravity between a millimetric droplet and a smooth solid or a liquid thin film. Solving coupled lubrication equations and analyzing the dominant terms in the solid- and liquid-film cases, we explain why the drainage is much faster in the liquid-film case, leading often to a shorter coalescence time, as observed in recent experiments.

drop | coalescence | film | drainage

Coalescence is a major process in multiphase flows, since it controls, with the break-up dynamics, the global evolution of the number of droplets and bubbles in the flow. It is therefore crucial for spray cooling and coating (1), viscous flows in capillaries (2, 3), emulsion and foams (4, 5), or droplet transmission of diseases (6, 7), for instance. Coalescence is in fact a complex phenomenon, the effective contact between two liquid bodies being not at all automatic as the interfaces approach each other, since surface interactions and viscous forces can, in particular, contribute to separate the interfaces (8–11). These forces can lead to the striking "floating drops" phenomena, as already mentioned by Lord Rayleigh (12) and Osborne Reynolds (13): For instance, it can be observed in an everyday life "experiment" by watching small coffee drops dancing in the mug above the liquid surface before sinking (14), or when a drop is deposited on a vibrating liquid bath (15, 16). The coalescence dynamics is controlled at first by the drainage of the thin fluid film separating the two liquid bodies, whether we consider drop–drop, drop–film, or drop–substrate coalescences. The drainage of this separating film determines the time for coalescence that can be defined as the time between the beginning of the drainage regime (where no motion is present but the drainage) to the time where the film ruptures so that the two liquid bodies enter in contact, or the liquid starts to wet the substrate. Such thin-film drainage follows a lubrication dynamics (17–23), where the viscosity of the surrounding fluid induces high pressure in the film that leads to the interface deformation and sometimes to the entrapment of an air bubble at coalescence, as observed in drop impacts, for instance (24, 25). However, the lubrication dynamics prevents mathematically the rupture of the film in finite time [at least when surface tension is present (26)], even when the film is squeezed, so that the final stage of coalescence has to involve additional physical mechanisms, dominant at microscopic or even nanoscopic scales. Usual suspects are van der Waals interactions (27), surface roughness, thermal fluctuations, Marangoni currents, and noncontinuum effects (28), although their precise implications remain largely an open question. Even if this final stage of the coalescence dynamics can thus exhibit high fluctuations, it can usually be described as a thickness cut-off below which the film rupture happens rapidly, so that the lubrication dynamics can be taken as the dominant

mechanism to determine the coalescence time. Eventually, even the drainage time can exhibit large variations in experiments and models, mostly poorly understood, so that it is crucial to have a better comprehension of the lubrication dynamics of drainage in the different configurations encountered (11, 29).

Drop coalescence (30–32) can be obtained through mainly two different practical configurations: drop collision (to another drop, a bath, or a substrate in particular), where the drop velocity is the main control parameter (33); and drop deposition, the situation considered in the present paper, where the drop is smoothly deposited on the substrate, meaning that its velocity is zero and that the weight of the drop only is leading to its coalescence with the substrate (29). While most of the experimental, numerical, and theoretical studies have focused on the drop/drop collision, only little attention has been paid eventually to the case of the deposition of a drop on a smooth liquid substrate, where the coalescence dynamics is almost quasistatic, since it is driven by the weight of the drop that squeezes the air gap between the drop and the wetted substrate. Recently, an experimental investigation of the coalescence of a millimetric drop gently laying on a thin viscous film (29) has revealed unexpected drainage dynamics: The drainage time is seen to be much shorter in the presence of a very thin viscous film than the time of touchdown estimated through simple lubrication arguments. The authors show experimentally that tangential flows at both interfaces between the gas and the liquids cannot be neglected, as it is often done in theory, allowing a more rapid drainage of the gas layer (34). These tangential flows are created by the viscous entrainment of the liquids by the gas layer that is squeezed, a mechanism also observed recently in Leidenfrost configuration (35). In order to elucidate the influence of these tangential flows in the drainage dynamics, the present study investigates the drainage dynamics of the thin air film squeezed between a weighting millimetric drop and a solid or wetted surface, thus varying the flow structure of the interstitial gas layer.

Significance

When a millimetric droplet is laying on a smooth surface, either liquid or solid, the slow gravity drainage of the air layer separating the surface from the drop leads to the entrapment of a thin bubble underneath. In this work, we investigate theoretically, and through numerical computations, the bubble-drainage dynamics on a solid and a liquid film. We show and explain how this dynamics before coalescence is much faster on a thin liquid film than on a solid surface.

Problem Formulation

We consider a liquid droplet landing gently on a wetted surface. The main question we want to address is thus: How long does it take for the two liquid surfaces to reach a threshold thickness (defined by the rupture mechanism) as the viscosity of the liquid film varies?

The liquid-film height is denoted by $h_1(r, t)$, and the local height of the droplet interface is $h_2(r, t)$, where r is the radial coordinate according to the axis of symmetry, and t is time. As seen in Fig. 1, the three domains (liquid film, gas film, and liquid droplet) are denoted, respectively, 1, 2, and 3, and every physical parameter (density, viscosity, etc.) will be noted with an index corresponding to the relevant region.

The drop is weighting on the thin gas and liquid films, creating a pressure field that exactly compensates the drops' weight (inertia can be neglected in the drainage regime). Viscous and pressure forces balance inside each film, creating viscous flows leading to their squeezing. We thus model the dynamics using the lubrication equation both in the gas and liquid films (domains 1 and 2 in Fig. 1), while a free slip boundary condition is taken at the interface between the drop and the gas film (19, 36). Indeed, considering a liquid motion inside the drop on the scale of the radius of the drop a, as experimentally reported in ref. 29, the tangential stress continuity across the gas film (of typical thickness $\bar{H}$) and the drop allows us to neglect the shear stress at the interface on the gas side as long as $(\eta_2/\eta_3)(a/\bar{H}) \gg 1$, which is the case in the experiments (29).

The weight of the drop is transmitted to the films through the interface normal stress condition, involving a pressure jump because of the surface tension. In the present study, for the sake of simplicity of the equations, we consider the two-dimensional (2D) version of the dynamics. It corresponds to assuming that axi-symmetric terms can be neglected, which is acceptable as soon as $\partial A/\partial r \gg A/r$, for any field $A(r, t)$, an approximation that is valid far from the symmetry axis, and thus particularly near the neck separating the entrapped gas bubble from the sur-

rounding, as argued, for instance, in ref. 37 in a similar context. Finally, in the lubrication approximation, we take the linearized curvatures for small slopes ($|\partial_r h| \ll 1$):

$$\kappa_1 \simeq \frac{\partial^2 h_1}{\partial r^2} \qquad \text{and} \qquad \kappa_2 \simeq \frac{\partial^2 h_2}{\partial r^2}.$$

Using lubrication theory in the two films, matching tangential velocities and shear stress between regions 1 and 2 and free slip boundary condition between regions 2 and 3, we obtain two coupled evolution equations for h_1 and $H \equiv h_2 - h_1$:

$$\frac{\partial h_1}{\partial t} = \frac{\partial}{\partial r}\left(\frac{h_1^3}{3\eta_1}\frac{\partial p_1}{\partial r} + \frac{h_1^2 H}{2\eta_1}\frac{\partial p_2}{\partial r} \right), \qquad [1]$$

$$\frac{\partial H}{\partial t} = \frac{\partial}{\partial r}\left(\frac{H^3}{3\eta_2}\frac{\partial p_2}{\partial r} + \frac{h_1 H}{2\eta_1}\left\{ h_1 \frac{\partial p_1}{\partial r} + 2H\frac{\partial p_2}{\partial r} \right\} \right). \qquad [2]$$

For each equation, one recognizes the usual lubrication term in the first term of the right-hand side, while the second term corresponds to the coupling between the two layers due to the tangential velocity boundary conditions. While in both films the gravity can be neglected (18), the coupling with the weighting drop is made through the pressure fields. Assuming small capillary numbers in the drop (in the experiments of ref. 29, the capillary numbers are always smaller than one, and mostly below 0.1), the pressure inside the drop can be taken purely hydrostatic, so that the pressure in the gas film (constant in z in the lubrication approximation) is given by Laplace's law:

$$p_2 = p_3(h_2) - \gamma\kappa_2 \simeq p_0 - \rho_3 g h_2 - \gamma\frac{\partial^2 h_2}{\partial r^2}, \qquad [3]$$

where p_0 is a reference pressure to be determined by the free-surface boundary condition at the top of the drop, and γ is the surface tension. The pressure in the liquid film (region 1) is also given by Laplace's law, yielding:

$$p_2 - p_1(h_1) = \gamma\kappa_1 \simeq \gamma\frac{\partial^2 h_1}{\partial r^2}. \qquad [4]$$

The fact that, within these approximations, we can neglect the influence of the velocity field in the drop for the pressure that is thus purely hydrostatic indicates that the deformation of the drop is driven only by the gravity field and the lubrication pressure beneath the drop. Therefore, the upper drop shape is simply that of a sessile drop, balancing surface tension with gravity. It means that, beside the region where the gas-film dynamics is relevant, the drop shape is static! This remark is crucial for solving numerically the system of equations above (Eqs. 1–4): As shown in Fig. 1, we introduce a distance R, large enough so that the lubrication pressure can be neglected. Actually, R is chosen such that the slope of the sessile top surface that patches the film interface at $r = R$ is of the order of unity (in the numerics shown here we have taken it equal to one, and we have checked that the results are mostly unchanged when varying this parameter around this value) (Fig. 1). The films Eqs. 1 and 2 are solved for $r < R$, while the drop shape is that of the static one outside this region (see more details in *Materials and Methods*).

The system of equations is controlled by the following dimensionless numbers, using for the typical radius of the drop the value of R computed using the slope 1 for the patching condition between the sessile drop and the gas layer/drop interface:

$$\text{Bo} = \frac{\rho_3 g R^2}{\gamma}, \quad \text{St}_1 = \frac{\eta_1}{\rho_3 R\sqrt{gR}}, \quad \text{St}_2 = \frac{\eta_2}{\rho_3 R\sqrt{gR}}.$$
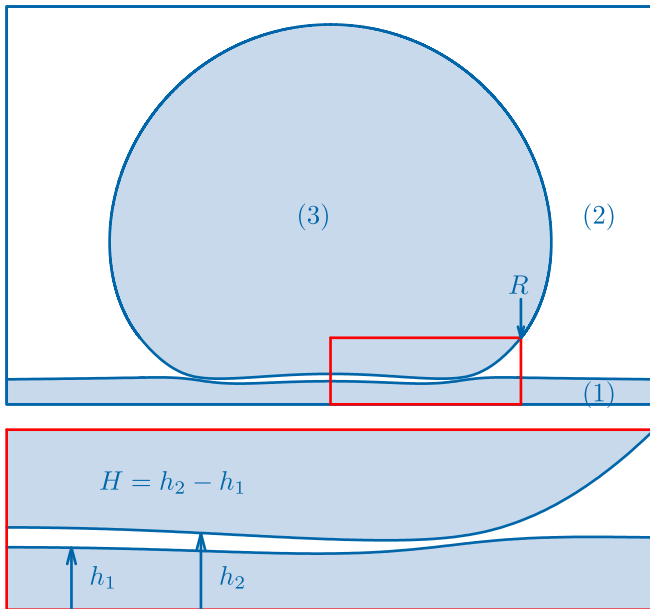

Fig. 1. Shape of a droplet lying on a thin liquid film. Underneath the drop, a gas dimple is entrapped, and the liquid film is deformed. The computational domain is defined as the radial extent $[0, R]$, where R is the radius at which the slope of the droplet interface equals one. The top surface of the drop corresponds to a static equilibrium shape, under the effects of gravity and surface tension.

The last dimensionless number is the ratio between the asymptotic thickness of liquid film $h_0 = \lim_{r \to \infty} h_1(r)$ and R:

$$\alpha = h_0/R.$$

In the present study, the Bond number Bo is assumed to have a moderate value, neither too big nor too small compared to one (Bo $= \mathcal{O}(1)$). Notice that the experiments described in ref. 29 correspond to significantly smaller droplets, with Bo $\simeq 0.36$ based on the equivalent radius of the droplet. In the following, we shall investigate the drainage dynamics as the parameters of the liquid film change, through the variation of our control parameter St_1. To dimensionalize the other parameters, we shall use typical values of the Stokes numbers from the experiments described in ref. 29: $St_2 = 1.25 \times 10^{-4}$ and $\alpha \simeq 0.02$. With these parameters, and after computing the top sessile drop, the value of R for all of the computations is $R \simeq 1.4$ mm. We will thus vary the liquid-film parameters, from the typical values of the experiments $St_1 \simeq 0.6$ toward the deposition on a solid substrate that can be accounted for simply in our equations by taking the limit $St_1 \to \infty$.

Typical interfaces profiles of the numerical solution of Eq. **1**, Eq. **2**, and the vertical force balance Eq. **25** are seen in Fig. 2 for two different configurations: On *Right*, the dynamics in the liquid-film case ($St_1 \simeq 0.6$) appears truly different from the solid case shown on *Left* ($St_1 = \infty$). We expect, therefore, the time of contact also to be different and to depend on St_1. The present paper aims, therefore, to understand how this contact time depends on the liquid-film properties, focusing on the influence of St_1 on the drainage of the air film.

Drainage Dynamics

In that purpose, we investigate and clarify first the dimple-drainage dynamics for these two characteristic cases $St_1 = \infty$ and $St_1 = 0.6$. Fig. 3 presents the evolution in time of the air gap H/R as a function of r/R. As for Fig. 2, *Left* corresponds to the solid substrate ($St_1 \to \infty$) and *Right* to the liquid film ($St_1 \simeq 0.6$). In both cases, the profiles correspond to $\tau = t \sqrt{g/R} = 0.7 \times 2^n$ with $n \in [0, 9]$ in dimensionless units (*Materials and Methods*).

After the dimple is formed, at short time, the drainage appears much faster in the case of a liquid film underneath. This fact is closely related to the continuity of tangential velocity across interface 1/2: In the solid case, this velocity is zero, whereas
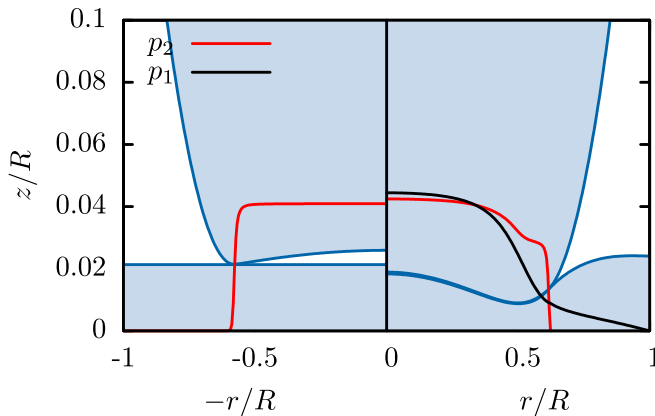

Fig. 2. Dimensionless droplet and film shapes h_2/R and h_1/R at the dimensionless time $\tau = t\sqrt{g/R} = 360$, in the case of a solid surface (*Left*; $St_1 = \infty$) and a liquid film (*Right*; $St_1 \simeq 0.6$). Parameters are as follows: Bo $= 1.01$, $St_2 = 1.25 \times 10^{-4}$. The red curve is the pressure in the gas film, and the black curve is the pressure in the liquid film (pressure scale is not indicated). At the pinch point, the pressure gradient in the liquid film is always much smaller than the pressure gradient in the gas film.

it is finite in the case of a liquid film. Therefore, viscous dissipation in the gas film at the tip of the dimple (where H is minimal) slows down more efficiently the dimple drainage, by contrast with the liquid-film case, where the gas can more easily escape from the dimple. Moreover, the liquid film deforms under the pressure field for finite St_1, so that the drop shape underneath and the film thickness almost coincide, as it can be seen in Fig. 2, *Right*.

Beside these qualitative observations, can we understand more quantitatively the dynamics of the dimple drainage in both cases? Fig. 4 shows the evolution with time for the two cases shown in Fig. 3 ($St_1 = 0.6$ and $St_1 = \infty$) of the two relevant quantities to describe the dimple geometry, $\bar{H}(t)$ the dimple mean height, defined below, and the minimal air gap, at the neck, $H_{\min}(t) = H(r_{\min}(t), t)$, where $r_{\min}(t)$ is its radial neck position (which is only slightly varying with time). Different scalings with time are observed in the asymptotic limit $t \to \infty$: For the solid substrate case $St_1 = \infty$ (black dashed lines), we have $\bar{H} \sim t^{-1/4}$ and $H_{\min} \sim t^{-1/2}$, while for the liquid film $St_1 = 0.6$ (blue solid lines), the dynamics follows $\bar{H} \sim H_{\min} \sim t^{-2/3}$.

To explain these scalings, let us first start with the solid case limit, where Eq. 2 reduces to the well-known lubrication equation:

$$\frac{\partial H}{\partial t} = \frac{1}{3\eta_2} \frac{\partial}{\partial r} \left(H^3 \frac{\partial p_2}{\partial r} \right) \qquad [5]$$

for which the drainage dynamics has been already characterized (20–23). We will recall the main results here for the consistency of our paper and also because it gives the framework for solving the finite St_1 cases. The interface geometry consists of a dimple of constant width, deflating slowly, connected to a small gap region, where viscous dissipation dominates, located in $r_{\min}$, that we can take constant when we approach the drainage time. We are looking for radial and vertical scalings of this small gap region, namely, $\ell(t)$ and $H_{\min}(t)$, respectively. In the dimple, the gas flux $Q = -\frac{H^3}{3\eta_2} \frac{\partial p_2}{\partial r}$ can be neglected, leading to a uniform pressure P_2. This is confirmed by Fig. 2, where the red curve on the left (solid case) corresponds to the pressure in the gas film. Integrating Eq. 3 twice according to r, where the gravity term can be neglected for the small dimple, we obtain $h_2(r)$, and, therefore H, assuming that $H(r_{\min}) \simeq 0$:

$$H(r, t) = \frac{3}{2} \frac{r_{min}^2 - r^2}{r_{min}^2} \bar{H}(t), \qquad [6]$$

where

$$\bar{H}(t) \equiv \frac{1}{r_{min}} \int_0^{r_{min}} H\,dr.$$

The curvature of the small gap region needs to be matched on its right to the curvature of the sessile top surface, yielding:

$$\frac{H_{\min}}{\ell^2} \sim \frac{1}{\ell_c}, \qquad [7]$$

where $\ell_c = \sqrt{\gamma/\rho_3 g}$ is the capillary length. Moreover, the decrease per unit time of the dimple surface S_d is equal to the leaking gas flux in the small gap. Indeed, integrating Eq. **5** between $r = 0$ and $r = r_{\min}$, we get for the surface decrease:

$$-\frac{dS_d}{dt} = -r_{min} \frac{d\bar{H}}{dt} = -\frac{H_{\min}^3}{3\eta_2} \frac{\partial p_2}{\partial r}, \qquad [8]$$

Remember that we do our analysis in 2D, but notice that the scalings would be unchanged in the three-dimensional analysis, since the self-similar dynamics is around a fixed radius r_{min}.
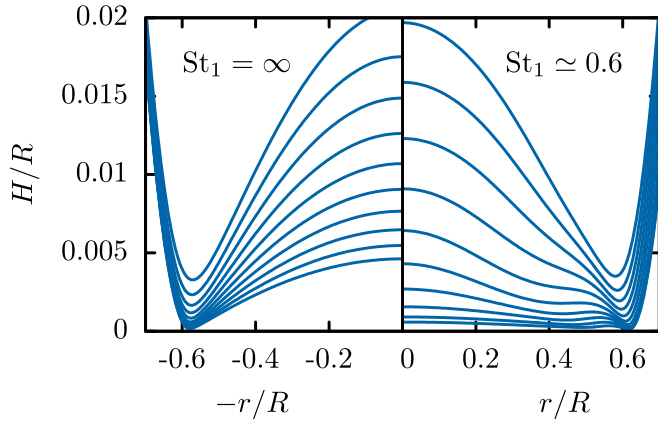
Fig. 3. Successive plots of the dimensionless gas-film height H/R in the case of a solid film ($St_1 \to \infty$; *Left*) and a liquid film ($St_1 = 0.6$; *Right*), for $\tau = t\sqrt{g/R} = 0.7 \times 2^n$ with $n \in [0, 9]$. Parameters are $Bo = 1.01$, $St_2 = 1.25 \times 10^{-4}$.

In the thin-gap region, the pressure gradient is large and given by Eq. **3**:

$$\frac{\partial p_2}{\partial r} \sim -\gamma \frac{\partial^3 H}{\partial r^3} \sim -\gamma \frac{H_{min}}{\ell^3}. \qquad [9]$$

Moreover, balancing the pressure in the dimple with the drop weight and integrating the pressure gradient across the neck gives the following relations:

$$P_2 \sim \frac{\rho_3 g R^2}{r_{min}} \quad \text{and} \quad r_{min} \sim Bo\ell_c, \qquad [10]$$

where we have used the fact that the scaling for the surface of our 2D drop is $S \sim R^2$, which is true for small to moderate Bond numbers. Using Eqs. **7**–**10**, we obtain:

$$\frac{d\bar{H}}{dt} \sim -\frac{\gamma H_{min}^4}{\eta_2 \ell^3 r_{min}} \sim -\frac{\sqrt{gR}}{Bo^{3/4}St_2}\left(\frac{H_{min}}{R}\right)^{5/2}. \qquad [11]$$

So far, we have only used lubrication theory and the matching of the curvature in r_{min} to the outer curvature given by the top sessile drop. To close the system of equations, we need a relation between the neck and the inner region. For the solid-film case, it can be done by matching the slopes between the dimple and the neck. Using the dimple geometry Eq. **6** and the length scales relevant in the neck, this matching yields in scaling:

$$\frac{H_{min}}{\ell} \sim \frac{\bar{H}}{r_{min}}, \qquad [12]$$

a result that could be obtained by using asymptotic matching between the two regions (38). Finally, using Eqs. **7**, **11**, and **12**, we obtain:

$$\ell \sim \frac{\bar{H}}{Bo}, \quad H_{min} \sim \frac{R}{Bo^{3/2}}\left(\frac{\bar{H}}{R}\right)^2, \qquad [13]$$

and

$$\frac{d\bar{H}}{dt} \sim -\frac{\sqrt{gR}}{Bo^{9/2}St_2}\left(\frac{\bar{H}}{R}\right)^5. \qquad [14]$$

Integrating Eq. **14** in time, we finally obtain the following long-time behaviors, already obtained, for instance, by (18):

$$\frac{\bar{H}}{R} \sim Bo^{9/8}St_2^{1/4}\tau^{-1/4}, \qquad [15]$$

$$\frac{H_{min}}{R} \sim Bo^{3/4}St_2^{1/2}\tau^{-1/2}, \qquad [16]$$

$$\frac{\ell}{R} \sim Bo^{1/8}St_2^{1/4}\tau^{-1/4}, \qquad [17]$$

where $\tau = t\sqrt{g/R}$ is the dimensionless time. These scalings in τ are confirmed by the numerical solution of Eqs. **1** and **2**, as seen in Fig. 4, where the dashed curves correspond to $\bar{H}/R$ and H_{min}/R in the limit $St_1 \to \infty$.

In the liquid case, we have to question the dominant balance in Eq. **2**. This balance is actually the same as for the solid case, for two reasons. The first one is that $|\partial p_2/\partial r| \gg |\partial p_1/\partial r|$ in the small gap region, as confirmed in Fig. 2. This is mainly due to surface tension that damps the high-curvature regions on the interface 1/2, and therefore smooths the pressure gradient. The other reason is that in our configuration, and in the experiments described in ref. 29, $St_2 \ll St_1$, such that the first term in the right-hand side of Eq. **2** is bigger than the third term, namely:

$$\left|\frac{H^3}{3\eta_2}\frac{\partial p_2}{\partial r}\right| \gg \left|\frac{h_1 H^2}{\eta_1}\frac{\partial p_2}{\partial r}\right|,$$

during our numerics. This condition gives, in fact, the validity range

$$H \gg \frac{\eta_2}{\eta_1}h_1, \quad \text{or} \quad \frac{H}{h_1} \gg \frac{St_2}{St_1},$$

for the scaling deduced below, suggesting that another scaling should be observed for smaller neck thickness than those computed numerically. Finally, the dominant balance in the lubrication Eq. **2** is still consistent with Eq. **5**. So, why are the self-similar scalings observed in Fig. 4 so different between the two cases? The answer lies in the fact that the scalings of H_{min} and $\bar{H}$ are no longer related through Eq. **12**, which is due to the matching between the parabolic dimple and the neck. For the liquid-film case, the dimple geometry is very different, showing a flatter structure (Fig. 3, *Right*), and our numerics suggest that the dynamics of H_{min} and $\bar{H}$ are similar:
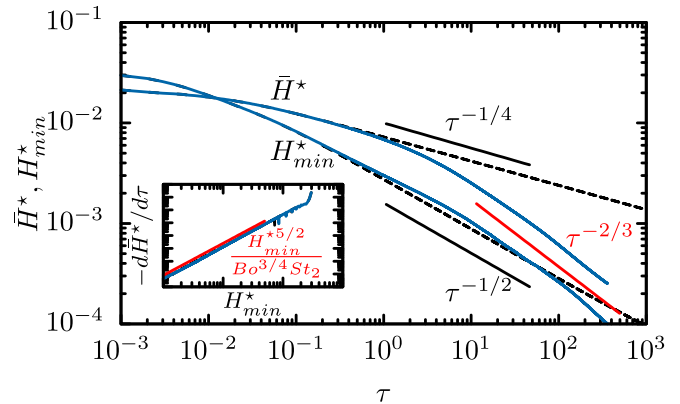

Fig. 4. Dimensionless mean height of the dimple $\bar{H}^\star = \bar{H}/R$ and minimum height $H_{min}^\star = H_{min}/R$ as a function of dimensionless time τ in the case of a liquid film ($St_1 = 0.6$; solid curves) and a solid film ($St_1 \to \infty$; dashed curves). (*Inset*) $-d\bar{H}^\star/d\tau$ as a function of $H_{min}^\star$ and the predicted law $H_{min}^{\star 5/2}/Bo^{3/4}St_2$. Ranges are $[10^{-4}, 10^{-1}]$ in x and $[10^{-7}, 10]$ in y. Solid case, black dashed curve; liquid-film case, blue solid curve.

$$H_{\min} \sim \beta \bar{H} \qquad [18]$$

up to a prefactor β that is a priori very small and depends on all the control parameters: Bo, St_1, St_2, and α. Using Eqs. **7** and **11**, which are still valid in the liquid-film case (since the curvature of the drop interface is much larger than the curvature of the film interface), and Eq. **18**, we obtain:

$$\frac{\bar{H}}{R} \sim Bo^{1/2} St_2^{2/3} \beta^{-5/3} \tau^{-2/3}, \qquad [19]$$

$$\frac{H_{min}}{R} \sim Bo^{1/2} St_2^{2/3} \beta^{-2/3} \tau^{-2/3}, \qquad [20]$$

$$\frac{\ell}{R} \sim St_2^{1/3} \beta^{-1/3} \tau^{-1/3}. \qquad [21]$$

These scalings in τ are again confirmed by numerical simulations, as seen in Fig. 4. The agreement, although very good, is not perfect because the dominant balance used in Eq. **2** is only an approximation here.

Moreover, our approaches to determine the scalings assume somehow a self-similar shape of the interface near the neck in the form:

$$H(r, t) \sim H_{\min}(t) F\left(\frac{r - r_{\min}}{\ell(t)}\right). \qquad [22]$$

Such self-similar character of the successive film thicknesses H, Eq. **22**, can be verified. In the solid case, from Eqs. **7** and **12**, we obtain $\ell \sim \bar{H}$ and $H_{\min} \sim \bar{H}^2$, while in the liquid-film case, from Eqs. **7** and **18**, we get $\ell \sim \bar{H}^{1/2}$ and $H_{\min} \sim \bar{H}$. Therefore, rescaling the radial and vertical coordinates of the interface around the neck according to these scalings allows us to check for spatial self-similarity, as seen in Fig. 5. The interface profiles rescale nicely near the neck for each case, while they do not at all in the dimple region. Remarkably, plugging this self-similar ansatz Eq. **22** into the lubrication Eq. **5** does not lead to the balance between the left- and the right-hand side of the equation for the scalings obtained above, showing in fact that the evolution of H_{min} is subdominant versus the mass flux terms. Indeed, neglecting the time-dependent and gravity terms in front of surface tension, we obtain the so-called "current equation":

$$F^3 F_{\xi\xi\xi} = C, \qquad [23]$$

where $\xi = (r - r_{min})/\ell(t)$ and C is a constant. This equation is studied in great detail in ref. 2, where we learn that the selected solution to this equation is usually the critical case, for which growth is quadratic on one side and linear on the other. This remark should be valid in the neck region, in both the liquid- and solid-film cases. We have verified this fact on the rescaled profiles shown in Fig. 5, and it turns out that, in both cases, the self-similar shape behaves like ξ toward the inner region (dimple) and ξ^2 toward the outer region (sessile drop), as indicated in the figure with red dots. This result is also consistent with the right and left matchings used to obtain the self-similarity exponents.

Contact Time

An interesting output of the present study, relevant to the recent experimental observations (29), is the time for the gas film to reach a thickness small enough such that coalescence can occur. Fig. 6 shows the dimensionless time it takes for the minimum gas-film dimensionless height $H_{\min}/R$ to reach a given value, as a function of the Stokes number St_1. The curves correspond to decreasing thresholds (from 10^{-3} to 4×10^{-4} from bottom to top). Finally, the two lines correspond to the solid case for a threshold 4×10^{-4} (dashed) and 3×10^{-4} (solid). Although the fluid cases exhibit a local maximum, for $1 \lesssim St_1 \lesssim 100$, even higher than the solid curve ($St_1 \to \infty$) for the minimal threshold (4×10^{-4}), we suspect that this local maximum disappears as the threshold decreases. Indeed, the lower threshold limit 3×10^{-4} in the solid case is well above the last curve for the liquid case. However, keeping in mind that we want to compare this length to a rupture-critical gas-layer thickness, it is interesting to notice that there could be an optimum value of the Stokes number St_1 for which the coalescence time is maximum. Although we do not have a definitive explanation for the existence of this maximum time to reach a given threshold, we would like to argue that this behavior comes from the competition between the gas-film drainage and the squeezing of the liquid film. Indeed, in this intermediate regime, the liquid film still deforms highly, so that the gas-film drainage is affected by the liquid-film geometry.

In order to estimate the drainage time before the film rupture, we need to estimate the typical length at which the physical mechanism for the rupture is pertinent. For the deposition on a liquid film, van der Waals forces (27) or noncontinuum effects (39) become relevant typically around and below 100 nm, leading (for a typical drop size of 1 mm) to a dimensionless threshold of 10^{-4} of the order of the smallest threshold investigated numerically in Fig. 6. On the other hand, for solid deposition, the roughness of the substrate is often the dominant mechanism for the film rupture. Taking a smooth substrate of roughness 1 μm, we obtain a dimensionless threshold of 10^{-3}. These estimates might explain why, although the drainage on a thin liquid film is faster than on a solid substrate, the coalescence time can be smaller for solid substrate, as observed eventually in experiments (29).

Conclusion

In this study, we have been investigating the drainage dynamics of a thin viscous liquid film squeezed by a millimetric droplet under gravity. We have shown a significant drainage speed-up when a liquid film covers the solid substrate, even if it is very viscous (Figs. 4 and 6). The drainage time can, therefore, vary by a few orders of magnitude as the viscosity of the liquid film changes. Nevertheless, the final coalescence time remains dependent of the final physical mechanism of the film rupture, and our approach allows for a quantitative prediction of the coalescence time when the threshold length scale is determined. Although our self-similar predictions (Eq. **22**) are probably difficult to measure experimentally, it would be very interesting to measure rigorously the coalescence time when varying the viscosity and the thickness of the liquid film. Moreover, we leave as a perspective of the present work parametric studies consisting of varying systematically these parameters, and the volume of the drop, through the Bond number.
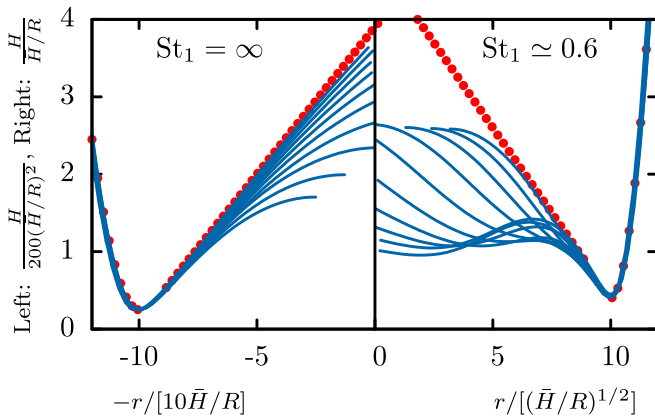

Fig. 5. Same profiles as in Fig. 3 rescaled according to $[10\bar{H}/R, 200(\bar{H}/R)^2]$ (solid case; *Left*), $[(\bar{H}/R)^{1/2}, \bar{H}/R]$ (liquid case; *Right*), and shifted horizontally in order for the neck to be at the same position for all profiles. The linear and quadratic behaviors corresponding to the critical solution of Eq. **23** are represented as red dots.
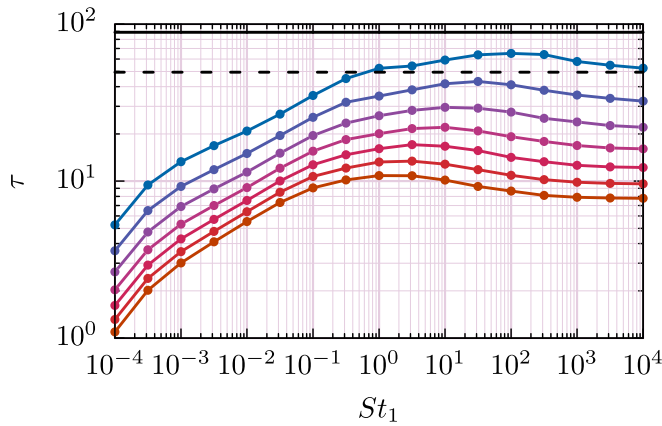
APPLIED PHYSICAL SCIENCES

Fig. 6. Dimensionless time τ for H_{min}/R to reach a given threshold (from 4×10^{-4} for blue to 10^{-3} for brown, with an increment of 10^{-4}). The black dashed and black solid lines correspond to 4×10^{-4} and 3×10^{-4}, respectively, in the solid case.

Materials and Methods

In order to solve numerically Eqs. **1** and **2**, we need boundary conditions in $r = 0$ and $r = R$. In $r = 0$, we use symmetric boundary conditions ($h_1' = h_1''' = 0$, $H' = H''' = 0$). In $r = R$, h_1 is matched onto an outer static meniscus, and H' is matched to its value given by the sessile top surface. The last condition for H is given by the vertical force balance:

$$\rho_3 \mathcal{S} g = \int_0^R p_2 dr = p_0(t)R - \rho_3 g R \overline{h_2} - \gamma \frac{\partial h_2}{\partial r}(R),$$ **[24]**

where we have used Eq. **3**, $\mathcal{S}$ is the surface of half of the drop (a surface in our 2D numerics in fact), and

$$\overline{h_2} = \frac{1}{R} \int_0^R h_2 dr.$$

p_2 is supposed to relax toward 0 in $r = R$:

$$0 = p_0 - \rho_3 g h_2(R) - \gamma \frac{\partial^2 h_2}{\partial r^2}(R),$$

giving p_0. Finally, we get an integral equation for h_2:

$$\frac{\mathcal{S}}{R} = h_2(R) + \frac{\gamma}{\rho_3 g} \frac{\partial^2 h_2}{\partial r^2}(R) - \frac{1}{R} \int_0^R h_2 dr - \frac{\gamma}{\rho_3 g R} \frac{\partial h_2}{\partial r}(R)$$ **[25]**

which is solved at each timestep, together with Eqs. **1** and **2**.

Eqs. **1–4** and **25** are made dimensionless according to the length scale R, velocity scale $\sqrt{gR}$, and pressure scale $\rho_3 V^2 = \rho_3 g R$. R is chosen to be the radial distance at which the slope of the sessile top surface is equal to 1

(Fig. 1). Plugging Eqs. **3** and **4** into Eqs. **1** and **2**, we obtain two nondimensional equations for $h_1^\star = h_1/R$ and $H^\star = H/R$ involving spatial derivatives of $h_1^\star$ and $H^\star$ up to the fourth derivative. We use a second-order, semi-implicit, finite-difference method, treating implicitly the spatial derivatives in the right-hand side of Eqs. **1** and **2**. Doing so, we get rid of the stiffness of these equations, coming from the high-order spatial derivatives (40, 41).

Eqs. **1** and **2** read, respectively, after dropping the $\star$:

$$\begin{aligned}
\frac{\partial h_1}{\partial \tau} = & \; h_2' \left(\frac{-h_1^2 h_1'}{St_1} - \frac{6 h_1 h_1' H + 3 h_1^2 H'}{6 St_1} \right) \\
& + h_2'' \left(\frac{-h_1^3}{3 St_1} - \frac{h_1^2 H}{2 St_1} \right) \\
& + h_2''' \left(\frac{-2 h_1^2 h_1'}{St_1 Bo} - \frac{6 h_1 h_1' H + 3 h_1^2 H'}{6 St_1 Bo} \right) \\
& + h_2'''' \left(\frac{-2 h_1^3}{3 St_1 Bo} - \frac{h_1^2 H}{2 St_1 Bo} \right) \\
& + H''' \left(\frac{h_1^2 h_1'}{St_1 Bo} \right) \\
& + H'''' \left(\frac{h_1^3}{3 St_1 Bo} \right),
\end{aligned}$$

$$\begin{aligned}
\frac{\partial H}{\partial \tau} = & \; h_2' \left(\frac{-H^2 H'}{St_2} - \frac{2 h_1 h_1' H + h_1^2 H'}{2 St_1} - \frac{2 h_1' H^2 + 4 h_1 H H'}{2 St_1} \right) \\
& + h_2'' \left(\frac{-H^3}{3 St_2} - \frac{h_1^2 H}{2 St_1} - \frac{h_1 H^2}{St_1} \right) \\
& + h_2''' \left(\frac{-H^2 H'}{St_2 Bo} - \frac{2 h_1 h_1' H + h_1^2 H'}{St_1 Bo} - \frac{2 h_1' H^2 + 4 h_1 H H'}{2 St_1 Bo} \right) \\
& + h_2'''' \left(\frac{-H^3}{3 St_2 Bo} - \frac{h_1^2 H}{St_1 Bo} - \frac{h_1 H^2}{St_1 Bo} \right) \\
& + H''' \left(\frac{2 h_1 h_1' H + h_1^2 H'}{2 St_1 Bo} \right) \\
& + H'''' \left(\frac{h_1^2 H}{2 St_1 Bo} \right),
\end{aligned}$$

where $h_2 = h_1 + H$ and $'$ denote differentiation according to r. For all of the computations presented in this article, the dimensionless spatial domain $r \in [0, 1]$ is discretized into 201 intervals, and the timestep is $\delta t = 10^{-3}$.

1. W. D. Ristenpart, P. M. McCalla, R. V. Roy, H. A. Stone, Coalescence of spreading droplets on a wettable substrate. *Phys. Rev. Lett.* **97**, 064501 (2006).
2. C. Lamstaes, J. Eggers, Arrested bubble rise in a narrow tube. *J. Stat. Phys.* **167**, 656–682 (2017).
3. Z. Li, L. Wang, J. Li, H. Chen, Drainage of lubrication film around stuck bubbles in vertical capillaries. *Appl. Phys. Lett.* **115**, 111601 (2019).
4. C. J. W. Breward, P. D. Howell, The drainage of a foam lamella. *J. Fluid Mech.* **458**, 379–406 (2002).
5. Z. Zapryanov, A. K. Malhotra, N. Aderangi, D. T. Wasan, Emulsion stability: An analysis of the effects of bulk and interfacial properties on film mobility and drainage rate. *Int. J. Multiphas. Flow* **9**, 105–129 (1983).
6. L. Bourouiba, E. Dehandschoewerker, J. W. M. Bush, Violent expiratory events: On coughing and sneezing. *J. Fluid Mech.* **745**, 537–563 (2014).
7. S. Poulain, L. Bourouiba, Disease transmission via drops and bubbles. *Phys. Today* **5**, 70 (2019).
8. G. Paul Neitzel, P. Dell'Aversana, Noncoalescence and nonwetting behavior of liquids. *Annu. Rev. Fluid Mech.* **34**, 267–289 (2002).
9. P. J. A. Janssen, P. D. Anderson, G. W. M. Peters, H. E. H. Meijer, Axisymmetric boundary integral simulations of film drainage between two viscous drops. *J. Fluid Mech.* **567**, 65–90 (2006).
10. R. H. Davis, J. A. Schonberg, J. M. Rallison, The lubrication force between two viscous drops. *Phys. Fluid. Fluid Dynam.* **1**, 77–81 (1989).
11. E. Klaseboer, J. P. Chevaillier, C. Gourdon, O. Masbernat, Film drainage between colliding drops at constant approach velocity: Experiments and modeling. *J. Colloid Interface Sci.* **229**, 274–285 (2000).
12. L. Rayleigh, Investigations in capillarity. *Philos. Mag.* **48**, 321 (1899).
13. O. Reynolds, On drops floating on the surface of water. *Chem. News* **44**, 211 (1881).
14. Y. Amarouchene, G. Cristobal, H. Kellay, Noncoalescing drops. *Phys. Rev. Lett.* **87**, 206104 (2001).
15. Y. Couder, E. Fort, C.-H. Gautier, A. Boudaoud, From bouncing to floating: Noncoalescence of drops on a fluid bath. *Phys. Rev. Lett.* **94**, 177801 (2005).
16. Y. Couder, E. Fort, Single-particle diffraction and interference at a macroscopic scale. *Phys. Rev. Lett.* **97**, 154101 (2006). .
17. D. Y. C. Chan, E. Klaseboer, R. Manica, Film drainage and coalescence between deformable drops and bubbles. *Soft Matter* **7**, 2235–2264 (2011).
18. S. G. Yiantsios, R. H. Davis, On the buoyancy-driven motion of a drop towards a rigid surface or a deformable interface. *J. Fluid Mech.* **217**, 547–573 (1990).
19. S. G. Yiantsios, R. H. Davis, Close approach and deformation of two viscous drops due to gravity and van der Waals forces. *J. Colloid Interface Sci.* **144**, 412–433 (1991).
20. S. P. Frankel, K. J. Myseis, On the "dimpling" during the approach of two interfaces1. *J. Phys. Chem.* **66**, 190–191 (1962).
21. S. Hartland, J. D. Robinson, A model for an axisymmetric dimpled draining film. *J. Colloid Interface Sci.* **60**, 72–81 (1977).

Duchemin and Josserand

22. S. Hartland, B. Yang, S. A. K. Jeelani, Dimple formation in the thin film beneath a drop or bubble approaching a plane surface. *Chem. Eng. Sci.* **49**, 1313–1322 (1994).
23. C-Y. Lin, J. C. Slattery, Thinning of a liquid film as a small drop or bubble approaches a solid plane. *AIChE J.* **28**, 147–156 (1982).
24. S. T. Thoroddsen, T. G. Etoh, K. Takehara, N. Ootsuka, A. Hatsuki, The air bubble entrapped under a drop impacting on a solid surface. *J. Fluid Mech.* **545**, 203–212 (2005).
25. S. T. Thoroddsen, M.-J. Thoraval, K. Takehara, T. G. Etoh, Micro-bubble morphologies following drop impacts onto a pool surface. *J. Fluid Mech.* **708**, 469–479 (2012).
26. L. Duchemin, C. Josserand, Curvature singularity and film-skating during drop impact. *Phys. Fluids* **23**, 091701 (2011).
27. W. W. Zhang, J. R. Lister, Similarity solutions for van der waals rupture of a thin film on a solid substrate. *Phys. Fluids* **11**, 2454–2462 (1999).
28. H. Lhuissier, E. Villermaux, Bursting bubble aerosols. *J. Fluid Mech.* **696**, 5–44 (2012).
29. H. Y. Lo, Y. Liu, L. Xu, Mechanism of contact between a droplet and an atomically smooth substrate. *Phys. Rev. X* **7**, 021036 (2017).
30. H. P. Kavehpour, Coalescence of drops. *Annu. Rev. Fluid Mech.* **47**, 245–268 (2015).
31. J. Eggers, J. R. Lister, H. A. Stone, Coalescence of liquid drops. *J. Fluid Mech.* **401**, 293–310 (1999).
32. Y. Yoon, F. Baldessari, H. D. Ceniceros, L. G. Leal, Coalescence of two equal-sized deformable drops in an axisymmetric flow. *Phys. Fluids* **19**, 102102 (2007).
33. J. Li, Macroscopic model for head-on binary droplet collisions in a gaseous medium. *Phys. Rev. Lett.* **117**, 214502 (2016).
34. A. F. Jones, S. D. R. Wilson, The film drainage problem in droplet coalescence. *J. Fluid Mech.* **87**, 263–288 (1978).
35. A. Bouillant *et al.*, Leidenfrost wheels. *Nat. Phys.* **14**, 1188–1192 (2018).
36. A. Oron, S. H. Davis, S. G. Bankoff, Long-scale evolution of thin liquid films. *Rev. Mod. Phys.* **69**, 931 (1997).
37. A. Perriot, J. R. Lister, A. B. Thompson, L. Duchemin, Shape and stability of axisymmetric levitated viscous drops. *J. Fluid Mech.* **617**, 167–185 (2008).
38. L. Duchemin, J. R. Lister, U. Lange, Static shapes of levitated viscous drops. *J. Fluid Mech.* **533**, 161–170 (2005).
39. L. Duchemin, C. Josserand, Rarefied gas correction for the bubble entrapment singularity in drop impacts. *C.R. Mecanique* **34**, 797–803 (2012).
40. T. Salez *et al.*, Numerical solutions of thin-film equations for polymer flows. *European Phys. J. E* **35**, 1–9 (2012).
41. L. Duchemin, J. Eggers, The explicit–implicit–null method: Removing the numerical instability of PDEs. *J. Comput. Phys.* **263**, 37–52 (2014).